Published online 1 December 2007

Nucleic Acids Research, 2008, Vol. 36, No. 4 ***e20***
doi:10.1093/nar/gkm1062

Measuring the dynamic surface accessibility of RNA with the small paramagnetic molecule TEMPOL

Vincenzo Venditti[1], Neri Niccolai[1] and Samuel E. Butcher[2,3,*]

[1]Biomolecular Structure Research Center and Dipartimento di Biologia Molecolare, Università di Siena, via Fiorentina 1, 53100 Siena, Italy, [2]Department of Biochemistry and [3]Nuclear Magnetic Resonance Facility at Madison, University of Wisconsin-Madison, 433 Babcock Dr. Madison, WI 53706, USA

Received September 11, 2007; Revised and Accepted November 8, 2007

ABSTRACT

The surface accessibility of macromolecules plays a key role in modulating molecular recognition events. RNA is a complex and dynamic molecule involved in many aspects of gene expression. However, there are few experimental methods available to measure the accessible surface of RNA. Here, we investigate the accessible surface of RNA using NMR and the small paramagnetic molecule TEMPOL. We investigated two RNAs with known structures, one that is extremely stable and one that is dynamic. For helical regions, the TEMPOL probing data correlate well with the predicted RNA surface, and the method is able to distinguish subtle variations in atom depths, such as the relative accessibility of pyrimidine versus purine aromatic carbon atoms. Dynamic motions are also detected by TEMPOL probing, and the method accurately reports a previously characterized pH-dependent conformational transition involving formation of a protonated C–A pair and base flipping. Some loop regions are observed to exhibit anomalously high accessibility, reflective of motions that are not evident within the ensemble of NMR structures. We conclude that TEMPOL probing can provide valuable insights into the surface accessibility and dynamics of RNA, and can also be used as an independent means of validating RNA structure and dynamics in solution.

INTRODUCTION

Surface accessibility plays a key role in delineating molecular interactions. However, accessible surface areas, calculated on the basis of static 3D structures, may not accurately describe the effective atom exposure to the bulk solution. In fact, dynamic features such as local flexibility (1,2), and/or hydration shell motions (3–5), have been observed to modulate surface accessibility in proteins.

Experimental studies on protein dynamics are, indeed, important in structural biology, and complement the otherwise 'static' view of molecular structure. In this respect, soluble paramagnetic probes have been shown to be useful in obtaining insight into processes regulating protein surface accessibility. In multidimensional NMR spectra, soluble paramagnetic molecules cause distance-dependent paramagnetic relaxation enhancement (PRE), manifested as line broadening and attenuation of cross-peak intensity. The extent of attenuation depends upon the local concentration of the paramagnetic probe. Thus, higher atom exposures result in higher degrees of paramagnetic attenuation (6,7). Recently, PRE studies have been widely applied in the investigation of protein–ligand (3), protein–protein (8–11) and protein–DNA(12) interactions, as well as in the localization of protein active sites (1,3,5,6,13,14). PRE studies are capable of efficiently detecting transient intermediates and short-lived encounter complexes that may otherwise go undetected by other methods (11,12).

The absence of strong interactions between biomolecules and paramagnetic probes is a prerequisite for probing surface accessibility. In the past few years, four paramagnetic agents with different sizes and chemical characteristics have been selected to fulfill this requirement: TEMPOL (3,5,6,7,15), Gd(III)DTPA-BMA (16), $Gd_2(L7)(H_2O)_2$ (10) and O_2 (2). Among these probes, TEMPOL has been used most extensively in protein accessibility studies, and a large amount of data on the mechanisms modulating the TEMPOL approach on protein surfaces is available (3,5,7,10,15,16). TEMPOL is soluble and small, with a radius of 3.7 Å (Figure 1A). Thus, TEMPOL is small enough to enter the narrow major groove of an RNA helix, and is therefore an ideal probe for investigating the surface accessibility of RNA. The paramagnetism of TEMPOL is due to the unpaired electron on the nitroxide group (Figure 1A), which induces fast relaxation of nuclear spins through electron-nuclear dipole–dipole coupling. In the absence

*To whom correspondence should be addressed. Tel: +1 608 263 3890; Fax: +1 6082623453; Email: butcher@biochem.wisc.edu

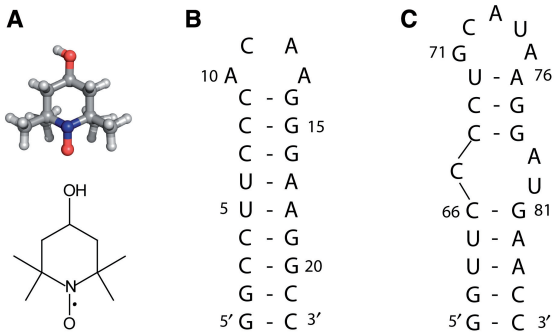

Figure 1. Structure of TEMPOL and secondary structures of the investigated RNAs. (**A**) TEMPOL, (**B**) HIV-1 RNA and (**C**) U6 ISL.

of specific interactions, TEMPOL approaches a molecular surface randomly, and thus the paramagnetic nitroxide group can be considered to be at the center of a sphere with a radius of 3.7 Å (the radius of TEMPOL). The paramagnetic effect of TEMPOL is exerted in a distance dependent, through-space manner, with >90% of relaxation induced through distances of 10 Å or less from the paramagnetic center (7).

Here, we show that TEMPOL induced PRE is a facile method that can be used to investigate the surface accessibility of RNA. For stable helical regions of RNA, there is excellent agreement between the surface accessibility and the position of the atom within the structure. Furthermore, we show that the method is capable of detecting dynamic conformational transitions. Some dynamic regions result in higher levels of PRE than would be predicted from the corresponding ensemble of NMR structures, suggesting that the method detects transient conformational dynamics that are 'invisible' with respect to the NMR-derived structures. Therefore, TEMPOL probing provides a facile way to independently validate and complement RNA structure models and dynamic measurements.

MATERIALS AND METHODS

Sample preparation and NMR measurements

The investigated RNA's, whose sequences are shown in Figure 1, were prepared by *in vitro* transcription as previously described (17,18). All NMR samples were ~1 mM in D_2O. The pH was adjusted to 6.8 for the HIV-1 RNA, and 8.0 and 5.7 for the U6 ISL RNA NMR samples. Paramagnetic samples contained an optimal 20 mM TEMPOL (4-hydroxy-2,2,6,6-tetramethylpiperidine-1 oxyl, 97% purity, Sigma-Aldrich) concentration, which was achieved by adding directly to the NMR tube a few microliters of a 2 M TEMPOL solution. Stock TEMPOL solutions were prepared by directly dissolving TEMPOL into 99.9% D_2O to a final concentration 2 M.

Since denaturing effects of TEMPOL on RNA structures could not be excluded *a priori*, after each addition of a 2 M solution of TEMPOL to the ~1 mM RNA solutions, 2D TOCSY spectra were recorded to check for chemical shift differences due to TEMPOL. No significant chemical shift changes upon TEMPOL addition were observed.

Conventional 2D TOCSY (40 ms mixing time), NOESY (150 ms mixing time) and ^{1}H-^{13}C HSQC spectra were acquired at the National Magnetic Resonance Facility at Madison (NMR-FAM) on Bruker DMX 600 and 750 MHz spectrometers. Data processing was carried out using XWINNMR 2.6 software (Bruker Biospin). Resonance assignments were performed on the basis of previously reported NMR data (BMRB entries: 5371, 5703, 5834, 6320 and 6543) (17–21). Resonance assignments were nonetheless accurately checked for diamagnetic and paramagnetic samples by standard procedures based on TOCSY and NOESY experiments.

Cross-peak volumes were measured with a greater than 90% confidence level using the Sparky integration tool (http://www.cgl.ucsf.edu/home/sparky).

Cross-peak attenuations

The cross-peak volumes were autoscaled according to the relation (13):

$$\upsilon_i^{p,d} = \frac{V_i^{p,d}}{(1/n)\sum_n V_i^{p,d}}$$

where $\upsilon_i^{p,d}$ is the autoscaled volume of peak i from the paramagnetic or diamagnetic spectra, $V_i^{p,d}$ is the measured peak volume from the paramagnetic or diamagnetic spectra, and n is the number of peaks measured. Hence the autoscaled volume is equal to the measured volume divided by a scaling factor corresponding to the mean cross-peak volume over n molecular locations. Paramagnetic attenuations, A_i's, were calculated from the autoscaled diamagnetic and paramagnetic peak volumes, respectively, υ^d and υ^p, according to the relation (13):

$$A_i = 2 - \frac{\upsilon_i^p}{\upsilon_i^d}$$

Depth index calculation

The 3D atom depths, reported as depth indexes $D_{i,r}$'s, were calculated on the basis of the NMR solution structures (PDB codes: 1PJY, 1SY4, 1SY7) (17,20,21) using the SADIC software (22). For each RNA, reported $D_{i,r}$'s were averaged over the whole NMR structure ensemble.

$D_{i,r}$ is defined according to the relation (22):

$$D_{i,r} = \frac{2V_{i,r}}{V_{o,r}},$$

where $V_{i,r}$ is the exposed volume of a sphere of radius r (sampling radius) centered on atom i and $V_{0,r}$ is the total volume of the same sphere. The sampling radius was set to 10 Å, which corresponds to the practical limit of the paramagnetic effect (7). The probe radius, used for the computation of the macromolecular surface, was set to 3.7 Å corresponding to the TEMPOL molecular radius as calculated by using the MOLMOL software (23). For

each C–H correlation, the entire ensemble of 20 NMR structures were analyzed and the averaged $D_{i,10}$ is reported. For simplicity, the averaged $D_{i,10}$ value is referred to in the text as D_i.

Molecular dynamics

Several MD simulations were performed in explicit solvent starting from the lowest energy solution structures of the investigated RNA's (PDB codes: 1PJY, 1SY4) (17,21,24) by using the AMBER package (25) and the AMBER-99 force field (26).

Each RNA was centered in a truncated octahedron and the initial shortest distance between the RNA atoms and the box boundaries was set to 10 Å. Then, an optimal amount of sodium ions was added in order to generate a neutral system. The remaining box volume was filled with TIP3P type water molecules (27). Water and ions positions were minimized with 500 steps of steepest descent plus 500 steps of conjugate gradient by keeping the RNA fixed. Then, the entire system was energy minimized with 1500 steps of steepest descent followed by 1000 steps of conjugate gradient minimization.

Then, each system was first equilibrated in a 20 ps run where temperature was gradually raised from 0 to 300 K. Hence, the equilibrated systems were simulated by keeping the temperature (300 K) and pressure (1 atm) constant. Thus, a weak coupling to external pressure baths was applied (relaxation time 1.0 ps) (28), while Langevin thermostat was used to control the temperature (collision frequency 1.0 ps^{-1}) (29). Bonds were constrained by SAHKE algorithm (30). Non-bonded interactions were accounted by using the PME method (31). An integration time step of 2 fs was used and trajectories were saved every 0.2 ps.

The backbone root mean square deviation (r.m.s.d.) of investigated RNA's over the MD runs (Figure S1, Supplementary Data) level off after equilibration periods shorter than 500 ps in all the cases. Thus all the subsequent analyses of the trajectories were carried out from 500 ps onward.

RESULTS

The stable HIV-1 frameshift site stem-loop

The frameshift site stem-loop RNA of HIV-1 is a highly conserved and very thermodynamically stable ($T_M > 90°C$) RNA domain (Figure 1B) (17,19,32). Due to its high stability and regular shape, it is a good initial model RNA to investigate the use of TEMPOL as a probe of RNA surface accessibility.

2D ^{1}H-^{13}C HSQC NMR spectroscopy is particularly suited for probing the macromolecular surface with TEMPOL, since the paramagnetic attenuation affects cross-peak intensities arising from covalently bound ^{13}C and ^{1}H nuclei that are very close in space (3). Furthermore, due to a favorable chemical shift dispersion, the aromatic CH correlations are suitable HSQC signals for delineating the accessibility of RNA structures. The TEMPOL generated PRE effects were analyzed for all the aromatic C2–H2, C6–H6 and C8–H8 correlations of the HIV-1 frameshift site RNA. The PRE values were quantitated as attenuation index (A_i) values, as described in the Materials and Methods section.

The TEMPOL induced A_i values were mapped to the surface of the RNA, and also plotted graphically (Figure 2A and B). The data correlate well with the structure of the HIV-1 RNA. The tetraloop and terminal ends of the RNA are more accessible than the A-form helical region, suggesting that 3D structure is the main factor modulating the surface accessibility of the RNA. Intriguingly, we noticed that the purine aromatic C8–H8 correlations have overall higher A_i values than the pyrimidine aromatic C6–H6 correlations. Quantitation of atom exposure, expressed as 3D atom depth index (D_i) (22) values, confirmed that the purine C8–H8 groups are more exposed than the pyrimidine C6–H6 groups by an average value of 8% over the interior of the helix (residues 2–8 and 15–21). The agreement between the average atom depth (D_i) calculated from the ensemble of NMR structures and attenuation index (A_i) is shown in Figure 2C. In general, CH groups having high D_i values, i.e. are close to the molecular surface, exhibit high A_i. In contrast, CH groups more buried in the structure have low or intermediate A_i values. This trend holds true even for nucleotides that have minor differences in atom exposure. For example, the first 5′ nucleotide is more accessible than the last 3′ nucleotide, even though they both reside at the helical end (Figure 2B). This is because the 5′ aromatic carbon (1C8, $D_i = 0.786$) is indeed more exposed than the 3′ aromatic carbon (22C6, $D_i = 0.491$), as indicated by its higher D_i value (Figure 2C). This is in agreement with chemical acylation studies showing that RNA helical 5′ ends are more accessible than 3′ ends (33). However, anomalously high A_i's are observed for nucleotides in the tetraloop region (A10, A12, A13 and G14), which is a less ordered region of the structure (17). In particular, the C8 groups of A12 and A13, corresponding to the 3′ side of the tetraloop, are highly attenuated, even though they are well stacked and relatively buried within the ensemble of NMR structures. These data suggest that the conformational variation within the time averaged NMR ensemble does not reflect the true conformational dynamics of the molecule. The NMR structures of RNA loop regions are largely defined by NOE distance restraints ($\leq$5 Å), and the unstacking of loop nucleotides may go undetected by NOE methods, since such transitions may result in internucleotide distances >5 Å. The paramagnetic attenuation of the tetraloop nucleotides suggests a strong connection between accessibility and RNA conformational flexibility.

To further investigate the accessibility–flexibility correlation, we performed a 10 ns MD simulation on the NMR structure of the HIV-1 frameshift site RNA (PDB code: 1PJY) (17). As expected, the root mean square fluctuations (r.m.s.f.) plot shows enhanced flexibility for the tetraloop and terminal nucleotides (Figure 3). In contrast, the helical residues experience limited and homogeneous fluctuations, consistent with the high stability previously observed for this RNA stem (19). By comparing the attenuation and the r.m.s.f. data (Figures 2B and 3), the

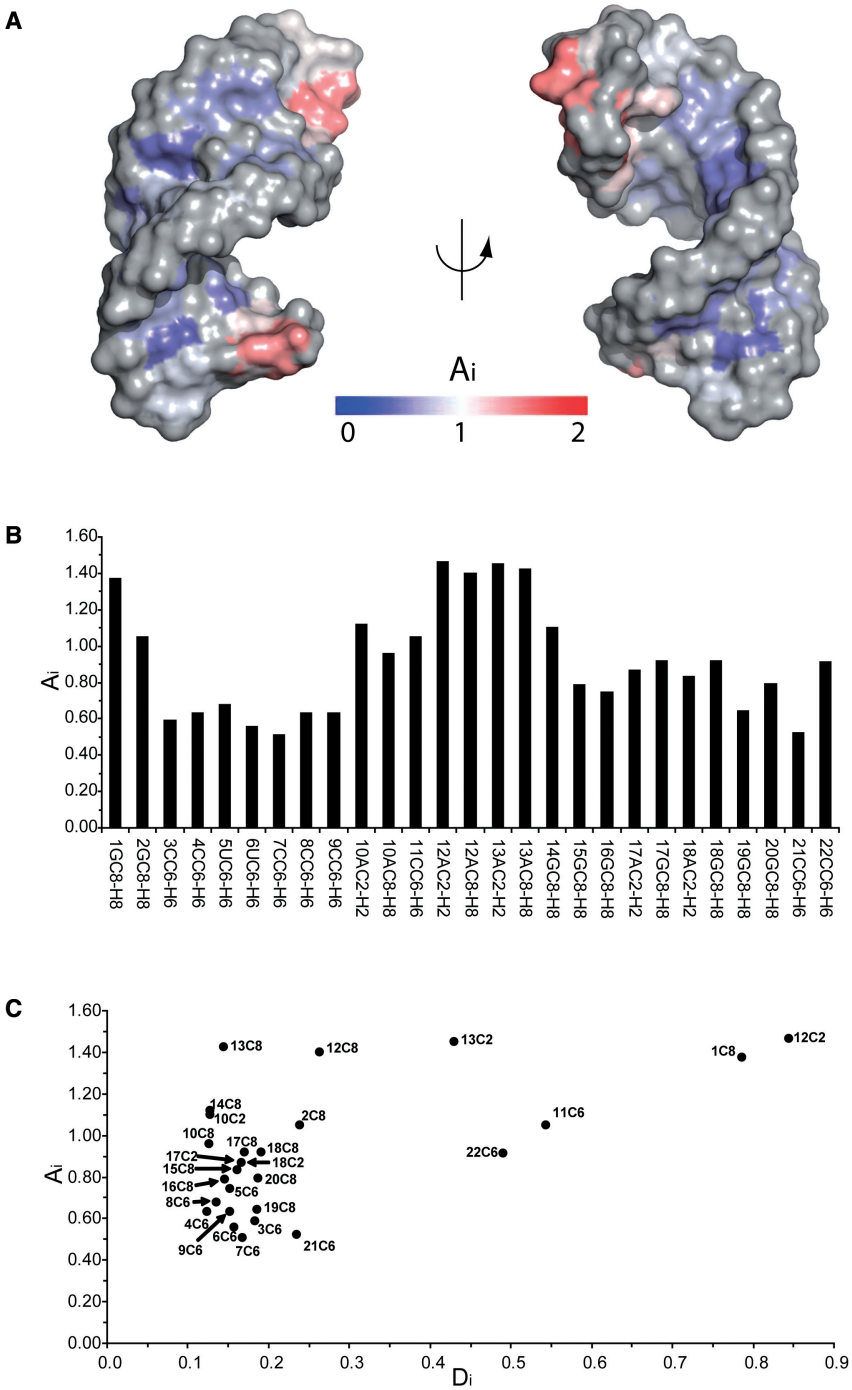

Figure 2. HIV-1 RNA surface accessibility. (**A**) Surface representation colored according to the observed attenuation (A_i). (**B**) Histogram of attenuation (A_i). (**C**) Paramagnetic attenuation (A_i) versus atom depth (D_i). Data are labeled according to the considered carbon atom.

correlation between accessibility and structural fluctuations is apparent.

The dynamic U6 intramolecular stem-loop

The U6 intramolecular stem-loop (ISL) is a highly conserved domain of the small nuclear U6 RNA (Figure 1C), and is involved in pre-messenger RNA splicing (34). The NMR solution structure determined at pH 7.0 (PDB code: 1SY4) (18,21) shows that the U6 ISL is comprised of two A-form helices separated by an internal loop containing a partially protonated C67–A79 wobble base pair and an unpaired U80 that is predominately stacked in the helix. The helix is capped by a GCAUA pentaloop that contains a sheared G71–A75 base pair and a 3′ adenine stack, facilitated by the bulged nucleotide U74. Hence, this RNA alternates between structured and

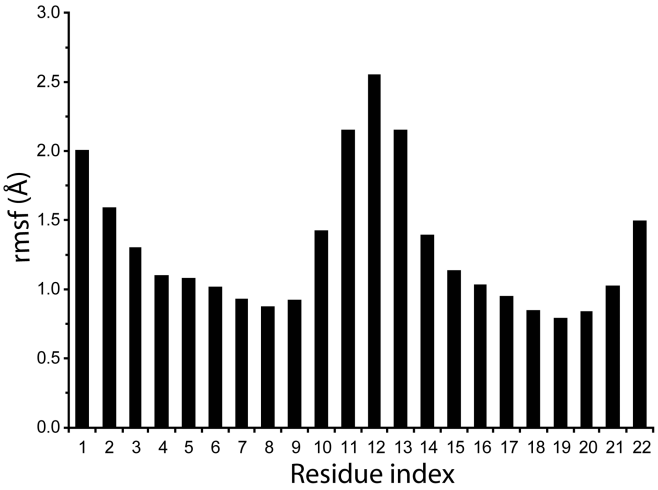

Figure 3. Histogram of root mean square fluctuations (r.m.s.f., Å) calculated from the 10 ns HIV-1 RNA MD simulation.

dynamic regions, enabling us to further investigate the relationship between accessibility and structural flexibility. Analyses of NMR line shapes and relaxation rates indicated that the U6 ISL RNA displays motions on both the ps–ns and μs–ms timescales (20,35). Furthermore, the U6 ISL undergoes a pH-dependent conformational switch induced by protonation of A79 (pKa = 6.5), which results in stabilization of the C67–A79 wobble pair and base flipping of the neighboring U80 nucleotide (20,21,35). The C67–A79 wobble pair has a lifetime of 20 μs, and the base flipping of U80 occurs on an ~80 μs timescale (20,35). Since the dynamics of this RNA have been previously characterized by NMR, it is an ideal model system for exploring the application of the TEMPOL PRE analysis in detecting RNA conformational transitions.

Since the pH-dependent conformational transition within the U6 ISL is directly correlated to the protonation state of A79 (35), the accessibility studies were performed at pH 8.0 and at pH 5.7. These experimental conditions assure minimal interference from the other conformer (population < 10%) (20). The TEMPOL PRE analysis was possible for 26/30 and 25/30 aromatic CH correlations, respectively, for the RNA at pH 8.0 and pH 5.7. The remaining resonances could not be reliably analyzed due to chemical shift overlap. The pH 8.0 attenuation profile (Figure 4A and B) correlates well with the U6 RNA structure. Higher A_i values are observed for the terminal nucleotides (62 and 85), the pentaloop and adjacent nucleotides (72–76; 71 was not measured due to spectral overlap), and the internal loop nucleotides (79 and 80).

Inspection of Figure 4C shows the good agreement between accessibility and atom exposure. All of the anomalously high A_i values are associated with nucleotides located in the dynamic pentaloop and internal loop regions (residues 73, 75, 76 and 79). The greatest anomaly is found for the A79 C2–H2 correlation, which experiences the highest TEMPOL accessibility at pH 8.0, in spite of its relatively low exposure in the pH 7.0 NMR solution structure. The A79 C2 atom is directly adjacent to the partially protonated nitrogen (A79 N1). Interestingly, the dynamics of protonation (20), as well as the relaxation rates for the base (35) suggest that A79 is indeed dynamic and must be accessible to solvent when unprotonated, although the solvent-accessible conformation could not be directly observed in the time-averaged ensemble of NMR structures calculated at pH 7.0 (20,35).

The conformational switch induced by lowering the pH to 5.7 caused changes in the TEMPOL PRE pattern which are mainly located in the internal loop region (Figure 5A and B). In particular, the most significant change is the large decrease in A_i (1.1–0.5) detected for A79 C8. This is in agreement with the structure and thermodynamics at pH 5.7 (20), which indicate that the internal loop structure is stabilized by formation of a protonated C67–A79 wobble pair at low pH, and that this base pair is fully stacked within the helix. Furthermore, an increase in A_i (1.1–1.4) is detected for U80 C6. The A_i value of 1.4 is consistent with an increase in the population of the base-flipped conformation for U80. As a comparison, the extrahelical U74 nucleotide experiences dynamics on the ps–ns timescale in a manner that is not pH-dependent (35) and has an A_i value that does not change with pH (Figure 5B). Additionally, the A_i values for the extrahelical nucleotides U74 and U80 are very similar at pH 5.7, and due to their extrahelical conformations, both nucleotides are also predicted to have high D_i values (Figure 5C). Although the increase in A_i for U80 correlates with an increased proportion of the base-flipped conformer at low pH, as expected (20), the increase in A_i for U80 relative to the pH 8.0 sample is less than might be expected, since the difference between the two measurements (0.3 A_i units) is barely above the observed standard deviation (Figure 5B). This is likely due to the fact that the pH 8.0 A_i value of 1.0 is relatively high, which may be reflective of the fact that a 3% population of based-flipped conformer still exists at this pH (35). Relative to the 80 microsecond base-flipping timescale (35), TEMPOL probing is very fast and results in irreversible PRE, allowing detection of even very transient populations. Therefore, the relatively small difference in A_i values (Figure 5B) for U80 is likely to be due to the detection of the base-flipped conformer even when it is present as a minor poplulation. On the other hand, the low pH condition locks A79 into a protonated wobble base pair with C67, which results in a more pronounced difference in attenuation for the A79 C2 and C8 resonances (Figure 5B). The flipped out U80 nucleotide may help shield A79 from TEMPOL, which could further account for the large drop in attenuation for the A79 C8–H8 correlation.

The A79 C2 resonance has an anomalously high A_i value at pH 8.0 (Figure 4C), suggesting that it is much more exposed than its position in the NMR structure, which was previously determined at pH 7.0 (21). Furthermore, interpretation of NMR relaxation rates at this site are complicated by chemical exchange due to the rapid protonation equilibrium of the adjacent N1 group (20,35). Therefore, in order to gain a better understanding of the dynamic motions associated with the unprotonated A79

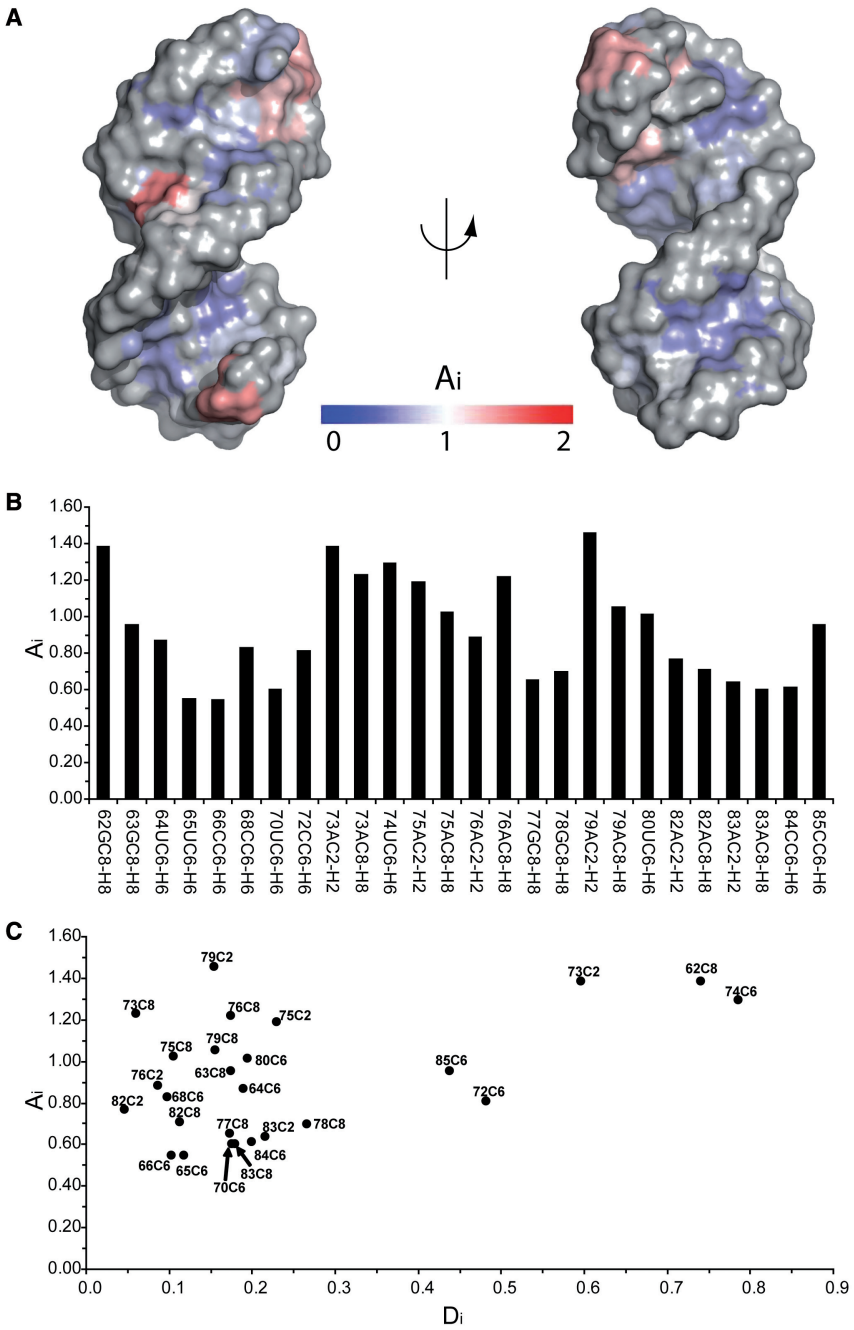

Figure 4. U6 ISL pH 8.0 surface accessibility. (**A**) Surface representation colored according to the observed attenuation (A_i). (**B**) Histogram of attenuation (A_i). (**C**) Paramagnetic attenuation (A_i) versus atom depth (D_i). Data are labeled according to the considered carbon atom.

conformation, an 18 ns MD simulation was performed starting from the pH 7.0 solution structure (PDB code 1SY4) (21) using the condition described in the Materials and Methods section. A low stability for the simulated trajectory can be observed by analyzing the RMSD versus time plot (Figure S1, Supplementary Data). In fact, during the MD trajectory, a switch from an unprotonated, single hydrogen bond C67–A79 wobble pair to a single hydrogen bond C67–U80 pair (C67 amino to U80 O4) is observed at the beginning of the simulation. This conformation was stable for ~3.5 ns, then underwent a base-pairing opening event for ~3 ns and subsequently reached a new base-pair conformation containing a double hydrogen-bonded C67–U80 pair (C67 amino-U80 O4, C67 N3-U80 imino) that was stable until the end of the simulation (Figure 6). This variation in the internal loop structure left A79 unpaired but still stacked in the helix. However, the MD sampling was not able to reach a stable orientation for this nucleotide that sampled many alternative conformations during the last 10 ns of trajectory. This behavior was also observed for an 11 ns MD simulation on a longer U6 ISL sequence (PDB code: 1XHP) (36), which has given similar

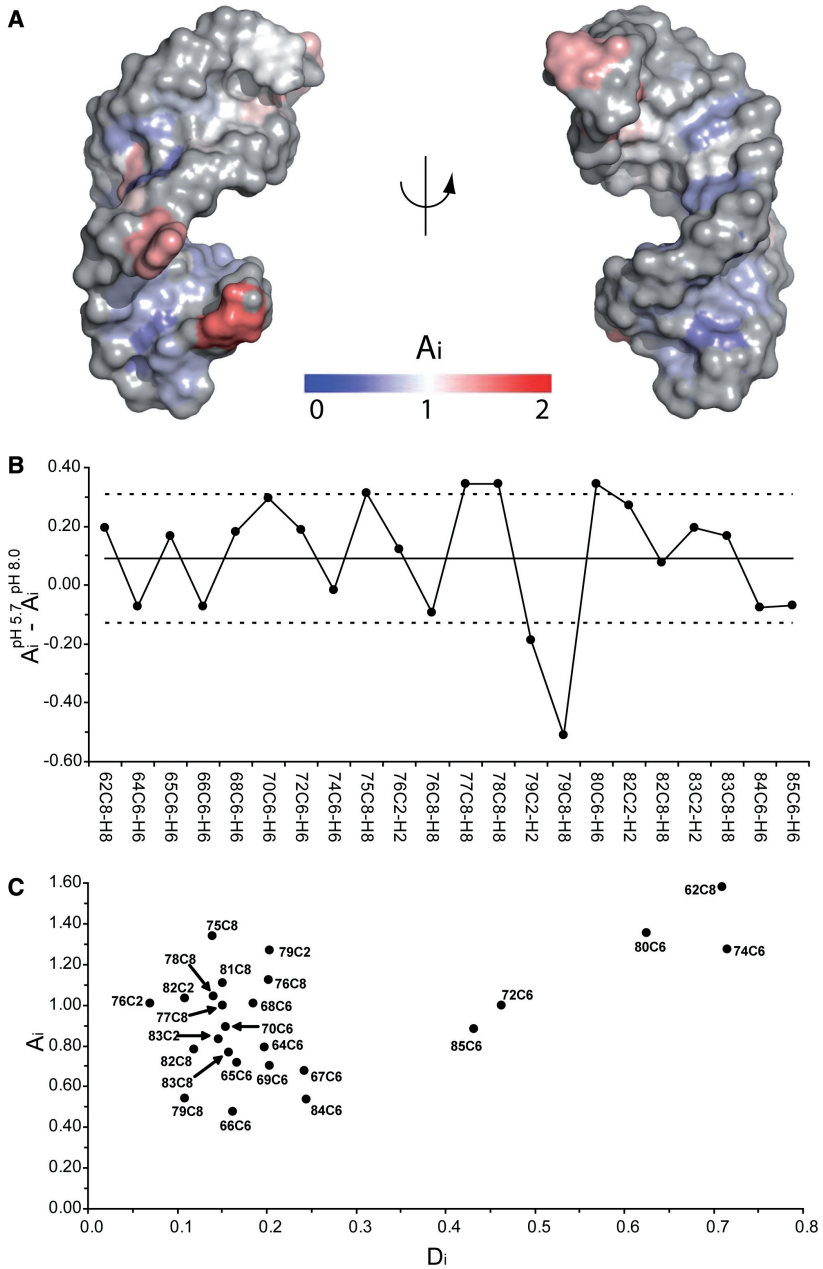

Figure 5. U6 ISL pH 5.7 surface accessibility. (**A**) Surface representation colored according to the observed attenuation (A_i). (**B**) A_i changes upon bulging out U80. Only A_i differences larger than the standard deviation (dashed lines) from the difference average (solid line) are referred to as large variations. The histogram of paramagnetic attenuations is supplied as Supplementary Data, Figure S3. (**C**) Paramagnetic attenuation (A_i) versus atom depth (D_i). Data are labeled according to the considered carbon atom.

results (Figure 6 and Figure S1, Supplementary Data). In order to relax the internal loop structure in the best local minimum, 10 conformations were extracted at regular intervals from the last 10 ns of simulation. Subsequently these structures were energy minimized using the simulated annealing protocol summarized in Figure S2, Supplementary Data. A comparison of the lowest energy MD-derived internal loop conformation and the lowest energy NMR solution structure is shown (Figure 7). In contrast to the pH 7.0 NMR structure, the unprotonated (high pH) internal loop forms a base triple in which C67 is no longer planar and A79 is rotated ~25° toward the minor grove. This conformation effectively increases the surface exposure of the A79 C2 group in a manner that is more consistent with the TEMPOL attenuation data ($D_{i,10}^{NMR} = 0.154$; $D_{i,10}^{MD} = 0.327$).

DISCUSSION

RNA surface accessibility

Investigating how soluble paramagnetic probes approach protein systems has been shown to provide useful information on the dynamic processes occurring at the

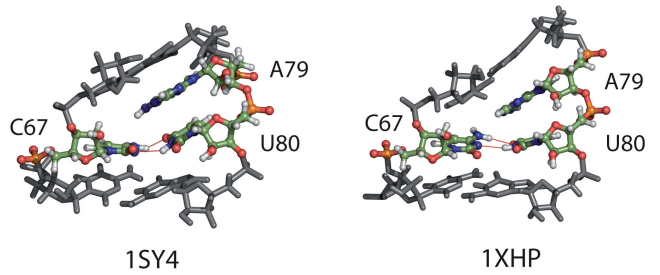

Figure 6. Snapshots of the MD simulations performed on two NMR structures (PDB codes: 1SY4 and 1XHP) of U6 ISL pH 7.0 conformer showing the internal bulge conformation.

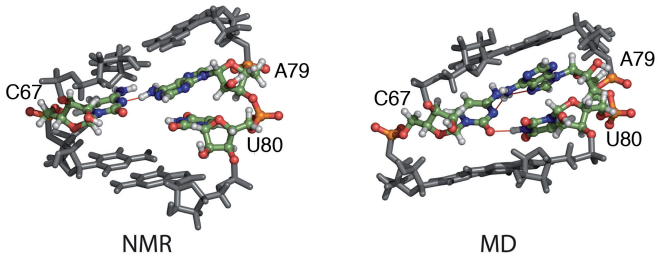

Figure 7. Comparison of the NMR and MD-derived U6 ISL internal-loop conformation. Hydrogen bonds are indicated with red lines.

protein–solution interface (1–3,5–10,14). Here, the surface accessibility of RNA molecules characterized by different shape and dynamics was analyzed by evaluating the PRE generated by TEMPOL on conventional 2D NMR measurements. The present results show that TEMPOL approaches RNA surfaces more uniformly than proteins (1,3,6,10,13,14). In fact, the agreement between the paramagnetic attenuation and atom depths for helical RNA molecules (Figures 2C, 4C and 5C), suggests that the shape, local dynamics and composition of RNA molecular surfaces are more homogeneous than those of proteins. Furthermore, the high negative charge typical of RNA surfaces may hamper formation of transient aggregates, which have been shown to significantly modulate the surface accessibility of proteins (5,8–10).

However, we find that nucleotides residing in flexible loop regions show higher accessibility than the ones observed for helical residues of similar depth (Figures 2–5). This finding suggests that these nucleotides transiently unstack, increasing the exposure of the base to the bulk solvent. In many cases, such transient events may not be evident within NMR structures that are typically time-averaged and population-weighted ensembles. Recently, the transient unstacking of stable GNRA tetraloops has been observed using femptosecond time-scale fluorescence spectroscopy (37).

Detecting RNA conformational changes

RNA conformational transitions are essential for ribosome and spliceosome function and play a significant role in recognition of proteins, RNA and ligands (38–41). Thus, studying RNA conformational dynamics is of primary relevance in understanding the correlation between RNA structure and function. However, investigating conformational changes in solution may be a complex and time-consuming endeavor. Hence, alternative methods able to map conformational transitions in RNA may be very helpful in complementing other investigation techniques. In the present report, we show that a small paramagnetic probe can detect a pH-dependent conformational switch in U6 RNA that has implications for spliceosome function and catalysis (20,35). The detailed pathway and associated energetics of this conformational change are unknown, but are driven by protonation of A79 (20,35). Here, we observe formation of the protonated C67–A79 pair causes large A_i variations in the internal loop region (Figure 5B). Comparison of the TEMPOL probing data (Figures 4 and 5) support the hypothesis that the transition between the protonated and unprotonated U6 ISL proceeds through an intermediate structure that is protonated but has a more exposed A79 (35). Interestingly, our MD simulation suggests a new conformation for the unprotonated U6 ISL internal bulge, in which the A79 base is rotated toward the minor grove, enhancing its solvent exposure (Figure 7). The MD simulation suggests that U80 is at least transiently involved in a base triple with C67 and A79. This may help explain the preference for this nucleotide to adopt a stacked conformation at high pH.

Further A_i variations are observed for nucleotides flanking the U6 ISL internal loop (G77 and G78) that show enhanced TEMPOL accessibility at low pH. These nucleotides are in stable Watson–Crick pairs, and previous thermodynamic investigations indicate that the structure is even more stable at low pH (21), dismissing the possibility of increased conformational flexibility for these nucleotides. Possibly, the modified molecular shape as well as the proximity of the highly dynamic loop nucleotides could increase the self-diffusion properties of the hydration layer surrounding these nucleotides, thus enhancing their accessibility to the paramagnetic probe (3–5,42).

Recently, we have demonstrated that TEMPOL probing can be used to detect the binding of a small molecule ligand to the surface of the HIV RNA (43). Therefore, the TEMPOL probing method is well suited for probing RNA structure, dynamics and ligand interactions.

SUPPLEMENTARY DATA

Supplementary Data are available at NAR Online.

ACKNOWLEDGEMENTS

This study made use of the National Magnetic Resonance Facility at Madison (www.nmrfam.wisc.edu), which is supported by National Institutes of Health grants P41RR02301 (Biomedical Research Technology Program, National Center for Research Resources) and P41GM66326 (National Institute of General Medical Sciences). Equipment in the facility was purchased with

funds from the University of Wisconsin, the National Institutes of Health (P41GM66326, P41RR02301, RR02781, RR08438), the National Science Foundation (DMB-8415048, BIR-9214394) and the US Department of Agriculture. This work was supported by NIH grants GM072447 and GM065166 to S.E.B. Funding to pay the Open Access publication charges for this article was provided by NIH grant GM065166 to S.E.B.

Conflict of interest statement. None declared.

REFERENCES

1. Scarselli,M., Bernini,A., Segoni,C., Molinari,H., Esposito,G., Lesk,A.M., Laschi,F., Temussi,P. and Niccolai,N. (1999) Tendamistat surface accessibility to the TEMPOL paramagnetic probe. *J. Biomol. NMR*, **15**, 125–133.
2. Teng,C.L. and Bryant,R.G. (2004) Mapping oxygen accessibility to ribonuclease a using high-resolution nmr relaxation spectroscopy. *Biophys. J.*, **86**, 1713–1725.
3. Niccolai,N., Spiga,O., Bernini,A., Scarselli,M., Ciutti,A., Fiaschi,I., Chiellini,S., Molinari,H. and Temussi,P.A. (2003) NMR studies of protein hydration and TEMPOL accessibility. *J. Mol. Biol.*, **332**, 437–447.
4. De Simone,A., Spadaccini,R., Temussi,P. A. and Fraternali,F. (2006) Toward the understanding of MNEI sweetness from hydration map surfaces. *Biophys. J.*, **90**, 3052–3061.
5. Venditti,V., Bernini,A., De Simone,A., Spiga,O., Prischi,F. and Niccolai,N. (2007) MD and NMR studies of [alpha]-bungarotoxin surface accessibility. *Biochem. Biophys. Res. Commun.*, **356**, 114–117.
6. Niccolai,N., Ciutti,A., Spiga,O., Scarselli,M., Bernini,A., Bracci,L., Di Maro,D., Dalvit,C., Molinari,H. *et al.* (2001) NMR studies of protein surface accessibility. *J. Biol. Chem.*, **276**, 42455–42461.
7. Teng,C.L. and Bryant,R.G. (2006) Spin relaxation measurements of electrostatic bias in intermolecular exploration. *J. Magn. Reson.*, **179**, 199–205.
8. Liepinsh,E., Baryshev,M., Sharipo,A., Ingelman-Sundberg,M., Otting,G. and Mkrtchian,S. (2001) Thioredoxin fold as homodimerization module in the putative chaperone ERp29: NMR structures of the domains and experimental model of the 51 kDa dimer. *Structure*, **9**, 457–471.
9. Bernini,A., Spiga,O., Ciutti,A., Venditti,V., Prischi,F., Governatori,M., Bracci,L., Lelli,B., Pileri,S. *et al.* (2006) NMR studies of BPTI aggregation by using paramagnetic relaxation reagents. *Biochim. Biophys. Acta*, **1764**, 856–862.
10. Bernini,A., Spiga,O., Venditti,V., Prischi,F., Bracci,L., Tong,A.P.L., Wong,W. T. and Niccolai,N. (2006) NMR studies of lysozyme surface accessibility by using different paramagnetic relaxation probes. *J. Am. Chem. Soc.*, **128**, 9290–9291.
11. Tang,C., Iwahara,J. and Clore,G.M. (2006) Visualization of transient encounter complexes in protein-protein association. *Nature*, **444**, 383–386.
12. Iwahara,J. and Clore,G.M. (2006) Detecting transient intermediates in macromolecular binding by paramagnetic NMR. *Nature*, **440**, 1227–1230.
13. Molinari,H., Esposito,G., Ragona,L., Pegna,M., Niccolai,N., Brunne,R.M., Lesk,A.M. and Zetta,L. (1997) Probing protein structure by solvent perturbation of NMR spectra: the surface accessibility of bovine pancreatic trypsin inhibitor. *Biophys. J.*, **73**, 382–396.
14. Niccolai,N., Spadaccini,R., Scarselli,M., Bernini,A., Crescenzi,O., Spiga,O., Ciutti,A., Di Maro,D., Bracci,L. *et al.* (2001) Probing the surface of a sweet protein: NMR study of MNEI with a paramagnetic probe. *Protein Sci.*, **10**, 1498–1507.
15. Zhou,N., Mascagni,P., Gibbons,W.A., Niccolai,N., Rossi,C. and Wyssbrod,H. (1985) Confirmation of the solution structure of tyrocidine a using perturbation of proton relaxation rates by nitroxide spin labels. *J. Chem. Soc., Perkin Trans.*, **2**, 581–587.
16. Pintacuda,G. and Otting,G. (2002) Identification of Protein Surfaces by NMR Measurements with a Paramagnetic Gd(III) Chelate. *J. Am. Chem. Soc.*, **124**, 372–373.
17. Staple,D.W. and Butcher,S.E. (2003) Solution structure of the HIV-1 frameshift inducing stem-loop RNA. *Nucleic Acids Res.*, **31**, 4326–4331.
18. Huppler,A., Nikstad,L.J., Allmann,A.M., Brow,D.A. and Butcher,S.E. (2002) Metal binding and base ionization in the U6 RNA intramolecular stem-loop structure. *Nat. Struct. Mol. Biol.*, **9**, 431–435.
19. Staple,D.W. and Butcher,S.E. (2005) Solution Structure and Thermodynamic Investigation of the HIV-1 Frameshift Inducing Element. *J. Mol. Biol.*, **349**, 1011–1023.
20. Reiter,N.J., Blad,H., Abildgaard,F. and Butcher,S.E. (2004) Dynamics in the U6 RNA intramolecular stem-loop: a base flipping conformational change. *Biochemistry*, **43**, 13739–13747.
21. Reiter,N.J., Nikstad,L.J., Allmann,A.M., Johnson,R.J. and Butcher,S.E. (2003) Structure of the U6 RNA intramolecular stem-loop harboring an SP-phosphorothioate modification. *RNA*, **9**, 533–542.
22. Varrazzo,D., Bernini,A., Spiga,O., Ciutti,A., Chiellini,S., Venditti,V., Bracci,L. and Niccolai,N. (2005) Three-dimensional computation of atom depth in complex molecular structures. *Bioinformatics*, **21**, 2856–2860.
23. Koradi,R., Billeter,M. and Wüthrich,K. (1996) MOLMOL: A program for display and analysis of macromolecular structure. *J. Mol. Graph. Model.*, **14**, 51–55.
24. Davis,J.H., Foster,T.R., Tonelli,M. and Butcher,S.E. (2007) Role of metal ions in the tetraloop-receptor complex as analyzed by NMR. *RNA*, **13**, 76–86.
25. Case,D.A., Cheatham,T.E., Darden,T., Gohlke,H., Luo,R., Merz,K.M., Onufriev,A., Simmerling,C., Wang,B. *et al.* (2005) The Amber biomolecular simulation programs. *J. Comput. Chem.*, **26**, 1668–1688.
26. Wang,J., Cieplak,P. and Kollman,P.A. (2000) How well does a restrained electrostatic potential (RESP) model perform in calculating conformational energies of organic and biological molecules? *J. Comput. Chem.*, **21**, 1049–1074.
27. Mohoney,M.W. and Jorgensen,W.L. (2000) A five-site model for liquid water and the reproduction of the density anomaly by rigid, nonpolarizable potential functions. *J. Chem. Phys.*, **112**, 8910–8922.
28. Berendsen,H.J.C., Postma,J.P.M., van Gunsteren,W.F. and Di Nola,A. (1984) Molecular dynamics with coupling to an external bath. *J. Phys. Chem.*, **91**, 6269–6271.
29. Pastor,R.W., Brooks,B.R. and Pastor,R.W. (1988) An analysis of the accuracy of Langevin and molecular dynamics algorithms. *Mol. Phys.*, **65**, 1409–1419.
30. Ryckaert,J.P., Ciccotti,G. and Berendsen,H.J.C. (1977) Numerical integration of the Cartesian equations of motion of a system with constraints: Molecular dynamics of n-alkanes. *J. Comput. Chem.*, **23**, 327–341.
31. Darden,T., Perera,L., Li,L. and Pedersen,L. (1999) New tricks for modellers from the crystallography toolkit: the particle mesh Ewald algorithm and its use in nucleic acid simulations. *Struct. Fold Des.*, **7**, R55–R60.
32. Hofacker,I.L., Fekete,M., Flamm,C., Huynen,M.A., Rauscher,S., Stolorz,P.E. and Stadler,P.F. (1998) Automatic detection of conserved RNA structure elements in complete RNA virus genomes. *Nucleic Acids Res.*, **26**, 3825–3836.
33. Weeks,K.M. and Crothers,D.M. (1993) Major grove accessibility of RNA. *Science*, **261**, 1574–1577.
34. Fortner,D.M., Troy,R.G. and Brow,D.A. (1994) A stem/loop in U6 RNA defines a conformational switch required for pre- mRNA splicing. *Genes Dev.*, **8**, 221–233.
35. Blad,H., Reiter,N.J., Abildgaard,F., Markley,J.L. and Butcher,S.E. (2005) Dynamics and metal ion binding in the U6 RNA intramolecular stem-loop as analyzed by NMR. *J. Mol. Biol.*, **353**, 540–555.
36. Sashital,D.G., Cornilescu,G., McManus,C.J., Brow,D.A. and Butcher,S.E. (2004) U2–U6 RNA folding reveals a group II intron-like domain and a four-helix junction. *Nat. Struct. Mol. Biol.*, **11**, 1237–1242.

37. Zhao,L. and Xia,T. (2007) Direct revelation of multiple conformations in RNA by femtosecond dynamics. *J. Am. Chem. Soc.*, **129**, 4118–4119.
38. Noller,H.F. and Baucom,A. (2002) Structure of the 70 S ribosome: implications for movement. *Biochem. Soc. Trans.*, **30**, 1159–1161.
39. Rodnina,M.V., Daviter,T., Gromadski,K. and Wintermeyer,W. (2002) Structural dynamics of ribosomal RNA during decoding on the ribosome. *Biochimie*, **84**, 745–754.
40. Valle,M., Zavialov,A., Sengupta,J., Rawat,U., Ehrenberg,M. and Frank,J. (2003) Locking and unlocking of ribosomal motions. *Cell*, **114**, 123–134.
41. Butcher,S.E. and Brow,D.A. (2005) Towards understanding the catalytic core structure of the spliceosome. *Biochem. Soc. Trans.*, **33**, 447–449.
42. De Simone,A., Dodson,G.G., Verma,C.S., Zagari,A. and Fraternali,F. (2005) Prion and water: tight and dynamical hydration sites have a key role in structural stability. *Proc. Natl Acad. Sci. U.SA*, **102**, 7535–7540.
43. Staple,D.W., Venditti,V., Niccolai,N., Elson-Schwab,L., Tor,Y. and Butcher,S.E. (2007) Guanidinio-neomycin B recognition of an HIV-1 RNA helix. *Chem. Biochem.*, In Press.